The Astrophysical Journal, 730:122 (10pp), 2011 April 1 doi:10.1088/0004-637X/730/2/122

CORONAL SEISMOLOGY USING EIT WAVES: ESTIMATION OF THE CORONAL MAGNETIC FIELD STRENGTH IN THE QUIET SUN

M. J. West[1], A. N. Zhukov[1,2], L. Dolla[1], and L. Rodriguez[1]
[1] Solar–Terrestrial Center of Excellence-SIDC, Royal Observatory of Belgium, Avenue Circulaire 3, B-1180 Brussels, Belgium; mwest@oma.be
[2] Skobeltsyn Institute of Nuclear Physics, Moscow State University, 119992 Moscow, Russia
Received 2010 December 17; accepted 2011 January 28; published 2011 March 11

ABSTRACT

Coronal EIT waves have been observed for many years. The nature of EIT waves is still contentious, however, there is strong evidence that some of them might be fast magnetosonic waves, or at least have a fast magnetosonic wave component. The fast magnetosonic wave speed is formed from two components; the Alfvén speed (magnetic) and the sound speed (thermal). By making measurements of the wave speed, coronal density and temperature it is possible to calculate the quiet-Sun coronal magnetic field strength through *coronal seismology*. In this paper, we investigate an EIT wave observed on 2009 February 13 by the SECCHI/EUVI instruments on board the *STEREO* satellites. The wave epicenter was observed at disk center in the *STEREO B* (Behind) satellite. At this time, the *STEREO* satellites were separated by approximately 90°, and as a consequence the *STEREO A* (Ahead) satellite observed the wave on the solar limb. These observations allowed us to make accurate speed measurements of the wave. The background coronal density was derived through *Hinode*/Extreme-ultraviolet Imaging Spectrometer observations of the quiet Sun and the temperature was estimated through the narrow temperature response in the EUVI bandpasses. The density, temperature, and speed measurements allowed us to estimate the quiet-Sun coronal magnetic field strength to be approximately 0.7 ± 0.7 G.

Key words: Sun: corona – Sun: fundamental parameters

Online-only material: color figures

1. INTRODUCTION

One of the most difficult tasks in coronal physics is measuring accurate coronal parameters such as magnetic field strength, temperature, and density, especially in the absence of in situ instruments. The magnetic field strength is particularly tricky to measure, as the usual methods, such as using Zeeman splitting of spectral lines and the Hanle effect, are complicated due to thermal broadening and polarization effects. However, some observations have been made with these method: Lin et al. (2000) and later Lin et al. (2004) used an infrared coronal emission line of Fe XIII to measure the weak Stokes *V* circular polarization profiles resulting from the longitudinal Zeeman effect, and measured the magnetic flux density above an active region (AR) to be between 4 and 33 G. Such techniques mainly focus on the stronger AR fields.

Indirect methods of estimating the coronal magnetic field rely on photospheric extrapolation techniques (e.g., Wang & Sheeley 1992; Liu & Lin 2008; Schrijver & De Rosa 2003; Metcalf et al. 2008), radio techniques (e.g., Subramanian et al. 2010; Ramesh et al. 2010) and coronal seismology (see Uchida 1970; Roberts et al. 1984). Extrapolation techniques such as the potential field source surface models can describe the three-dimensional structure of the field in the corona from photospheric field maps, but are subject to errors due to electric currents and non-force free conditions.

Coronal seismology uses observations of waves propagating through the corona to estimate coronal characteristics, and can be separated into two broad fields of study, which cover global and local coronal seismology. The first relies on the assumption that there is a magnetohydrodynamic (MHD) wave dispersion relation that relates the frequency and the plasma properties (Cargill 2009). Two examples of suspected MHD waves are the Moreton wave observed in Hα images Moreton (1960) and the EIT wave, named after the Extreme ultraviolet Imaging Telescope (Delaboudinière et al. 1995) with which they were first observed. The second coronal seismology method relies on the observation and simulation of individual loops and loop bundles, and the solution of wave mode oscillations to infer plasma properties (see Nakariakov et al. 1999; Roberts et al. 1984). It is the former method that is used in this paper.

Images of transient bright fronts propagating through the coronal medium following an eruption were first obtained by EIT on the *Solar and Heliospheric Observatory* (*SOHO*) around 1997 (Moses et al. 1997; Dere et al. 1997b; Thompson et al. 1998). The propagating bright fronts often originate from erupting ARs and have wave-like appearances. The waves were predominantly observed through EIT's Fe XII 195 Å bandpass, suggesting a temperature preference for the phenomena. However, various authors have presented observations in other EUV wavelengths (see Wills-Davey & Thompson 1999; Zhukov & Auchère 2004; Long et al. 2008).

EIT waves have been observed with various speeds, generally ranging between 100 and 500 km s^{-1} (Thompson et al. 1999; Thompson & Myers 2009). However, the speed is often non-isotropic along a wave front of an individual event. The waves have been observed to propagate over both short and long distances (a few megameters to solar radii), and dispersion is often the cause of loss of visibility. It is also unclear if there is a relationship between the wave front intensity and the propagation speed.

The waves emanate from ARs, which are often flaring, and have a close association with several other phenomena, especially with coronal mass ejections (CMEs) which often share similar propagation angles as the waves (Biesecker et al. 2002). They also have a strong correlation with coronal dimmings and

may have a chromospheric counterpart observed as Moreton waves (Moreton 1960) observed in Hα data (see Warmuth et al. 2001).

EIT waves often fan out as they travel, but generally have a limited angular width. They propagate in a particular direction, and only change direction if they encounter a strong magnetic obstacle (e.g., Gopalswamy et al. 2009). However, there are observations of waves with large angular widths, and even halo events where the wave propagates in all directions from the source region (see Thompson et al. 1998, 1999). Such events are of a small percentage, and it is unknown if this is a consequence of the magnetic field characteristics, the density structure or instruments being unable to detect parts of wave fronts with lower intensity.

The nature of the EIT wave is still heavily contested, which is discussed in two recent papers by Wills-Davey & Attrill (2009) and Gallagher & Long (2010). The range in observed characteristics has allowed several interpretations of the waves. These can roughly be separated into two groups: wave solutions and non-wave solutions. Most wave explanations are based around the fast magnetosonic wave solution (Thompson et al. 1999), whereas the non-wave solutions cover several ideas including the wave being the successive opening of magnetic field lines (Chen et al. 2002) and current sheet heating between the erupting flux rope and surrounding field (Delannée et al. 2008).

Understanding the nature of the wave is fundamental to global coronal seismology, where speed measurements can be used to infer other coronal characteristics. Several reviews and discussions on this subject have been made (see Banerjee et al. 2007; De Moortel & Pascoe 2009; Nakariakov et al. 1999). There is significant evidence that at least some EIT waves are true fast-mode MHD waves (Wills-Davey & Thompson 1999; Patsourakos & Vourlidas 2009; Kienreich et al. 2009; Veronig et al. 2010). Uchida published a series of papers (Uchida 1968, 1970; Uchida et al. 1973) modeling Moreton waves observed in Hα images as fast magnetosonic waves using a Wentzel–Kramers–Brillouin approximation wave model. The results from the model were comparable to observations, especially the speed of the wave. Wang (2000) used a similar model for EIT waves, also producing comparable results. Later Wu et al. (2001) and Schmidt & Ofman (2010) produced full three-dimensional numerical simulations of EIT waves, both of which produced results that broadly simulated an EIT waves propagation.

The fast-mode model has several desirable characteristics; first, the wave is able to travel at right angles to the magnetic field, and there is evidence that waves form reasonably low in the solar atmosphere Patsourakos & Vourlidas (2009), where the field is largely perpendicular to the solar surface. Second, the wave is compressional (i.e., changes the density and the magnetic field magnitude), and a gradient in the magnetic field will cause the wave to change direction (see Uchida 1968; Wang 2000). Wills-Davey & Thompson (1999) first presented *Transition Region and Coronal Explorer* (Handy et al. 1999) high cadence observations of an EIT wave and presented observations of a wave inducing loop oscillations, and the wave refracted around magnetic structures. Later, Gopalswamy et al. (2009) presented observations of a wave reflecting off of a coronal hole.

In this paper, we study an EIT wave/CME eruption observed on 2009 February 13 (Figure 1). We present measurements of the speed and estimates of the temperature made with the Extreme-Ultraviolet Imagers (EUVI; Wuelser et al. 2004), which are a part of the Sun Earth Connection Coronal and Heliospheric Investigation (SECCHI) suite (Howard et al. 2008) on board the *Solar TErrestrial RElations Observatory* (*STEREO*) mission satellites (Kaiser et al. 2008). We also present density measurements of the quiet Sun made with the *Hinode*/Extreme-ultraviolet Imaging Spectrometer (EIS; Culhane et al. 2007). These observations are then used with the fast-mode magnetosonic interpretation of the wave to estimate the coronal magnetic field strength in the quiet-Sun regions.

In Section 2, we present our method for estimating the magnetic field. In Section 3, we present observations of the wave and derivation of coronal parameters, showing how the fortunate positioning of the EIS slit in relation to the wave provides us with accurate background measurements of the quiet-Sun density. Finally, in Section 5 we discuss the results and some of the limitations with the technique.

2. METHOD

In a linear approximation, the general form of the fast-mode wave speed in plasma is given by

$$v_f^2 = \frac{1}{2}\left[v_A^2 + c_s^2 + \sqrt{\left(v_A^2 + c_s^2\right)^2 - 4v_A^2 c_s^2 cos^2\theta}\right], \quad (1)$$

where $v_A = B/(4\pi\rho)^{\frac{1}{2}}$ is the Alfvén speed, $c_s = (\gamma P/\rho)^{\frac{1}{2}}$ is the local sound speed, ρ is the mass density, P is the plasma pressure, $\gamma = 5/3$ is the adiabatic index, and θ is the angle between the wave vector and the magnetic field **B**. As the dependence on θ is relatively weak, and the field can be considered largely perpendicular to the wave vector in the lower atmosphere, Equation (1) reduces to

$$v_f^2 \approx v_A^2 + c_s^2. \quad (2)$$

Or, by substituting the Alfvén and sound speeds into Equation (2) and rearranging we can estimate the magnetic field strength to be

$$B = \left(4\pi\left(\rho v_f^2 - \gamma P\right)\right)^{\frac{1}{2}}. \quad (3)$$

By substituting the ideal gas law for pressure of a fully ionized hydrogen plasma,

$$P = 2nk_B T, \quad (4)$$

into Equation (3), we find the magnetic field strength becomes a function of the wave speed, the temperature and the density, where n is the electron number density ($\rho = n \times m_p$ in the fully ionized hydrogen plasma where m_p is the proton mass) and k_B is the Boltzmann constant. Therefore, by calculating these parameters we can estimate the magnetic field strength, and the plasma β,

$$\beta = \frac{8\pi P}{B^2}. \quad (5)$$

How we obtain these quantities will be described in Section 3.

3. OBSERVATIONS

An EIT wave observed with the *STEREO* satellites on 2009 February 13 was analyzed. The wave emanated from NOAA AR 1012 and was first seen at 05:35 UT in the 195 Å bandpass (Figure 1). The wave was associated with a GOES B2 class flare and a CME with a speed around 340 km s^{-1}. The event

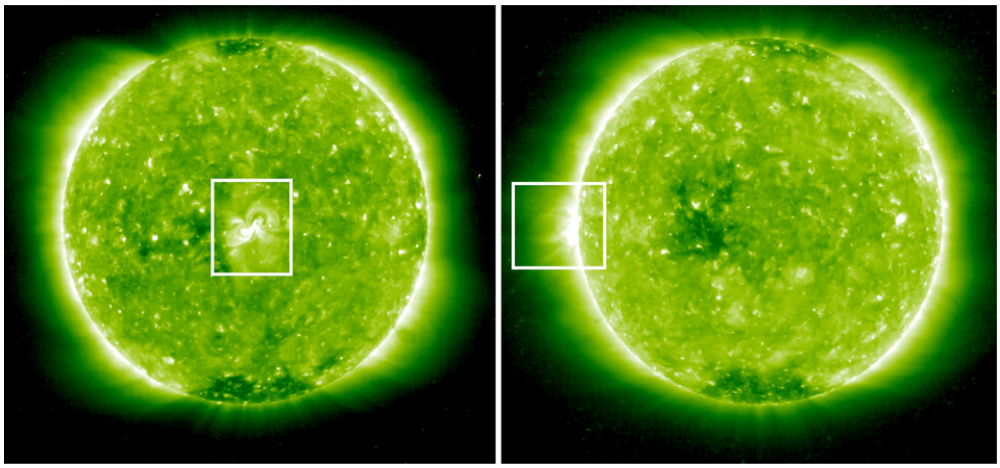

Figure 1. *STEREO B* (left) and *STEREO A* (right) 195 Å SECCHI/EUVI images at 05:35 UT on 2009 February 13. NOAA AR 1012, the source of the EIT wave under investigation, is highlighted by a white box. Due to the 90° angular separation of the *STEREO* satellites, the AR is seen on-limb in *STEREO A*, and in the center of disk in *STEREO B*.

(A color version of this figure is available in the online journal.)

also had associated dual dimmings behind the wave front. The event has already been presented in several papers (Patsourakos & Vourlidas 2009; Kienreich et al. 2009; Cohen et al. 2009). In this work, images from the *STEREO*/EUVI telescopes are used to study the wave dynamics and *Hinode*/EIS observations to measure the background quiet-Sun density.

3.1. STEREO SECCHI Observations

The *STEREO* mission is composed of two satellites: *STEREO A* (hereafter ST-A) orbiting the Sun ahead of the Earth in its orbit and *STEREO B* (hereafter ST-B) behind the Earth. Both satellites are gradually moving away from the Earth in their orbits, as well as away from each other. Therefore, the angular separation between the satellites increases with time, with the Earth roughly centered between them. On February 13, the *STEREO* spacecraft was separated by ≃90° (Figure 2). Each *STEREO* satellite carries a SECCHI instrument suite, including EUVI and the COR1 coronagraph imagers (Thompson et al. 2003). Figure 1 shows the two *STEREO* perspectives of the NOAA AR 1012 in EUVI 195 Å images.

A series of EUVI 195 Å/COR1 running difference images (the previous image subtracted) of 2009 February 13 wave can be seen in Figure 3. Changes in intensity are seen as bright and dark regions. Each image is composed of two parts: an EUVI ST-B image of the wave located on disk and an EUVI ST-A image superimposed on a COR1 coronagraph difference image, showing the wave on the limb. Both ST-A and ST-B images were taken at the same time, with the EUVI ST-B image time indicated.

Pre-flare conditions were observed at 05:25 UT (Figure 3(a)). The EIT wave is first seen at 05:35 UT (Figure 3(b)) around the source AR. In later images, the wave is observed to have a lower emission to the east. In ST-B, the wave is seen to move to the north and south concurrently. The wave is visible on disk until around 06:35 UT (Figure 3(h)). The circular shape of the wave seen in ST-B is believed to be the ground track signature of the expanding dome-shaped wave observed in ST-A, with increased emission at the edge due to the imager looking through a larger column of density (Ma et al. 2009).

The wave is visible in several EUVI passbands, as shown in Figure 4. The wave is most visible in the 195 Å passband observations, and to a lesser extent in the 171 Å and 284 Å

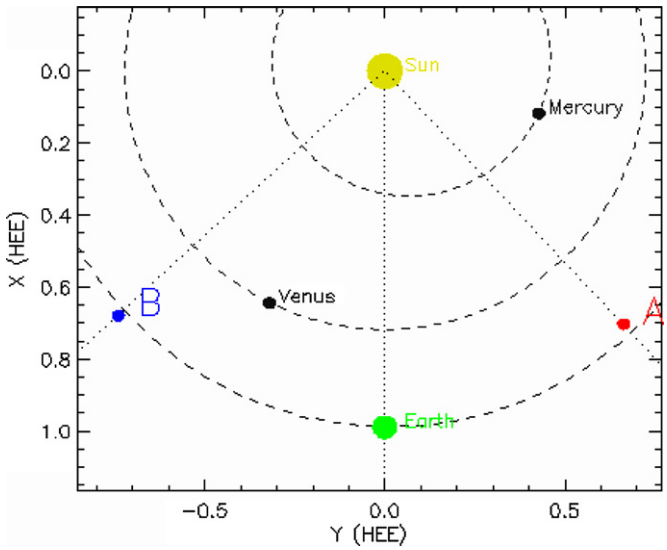

Figure 2. Schematic image of the *STEREO* satellites position relative to each other and the Earth. On 2009 February 13, the satellites were separated by ≃90° (source: Stereo Science Center).

(A color version of this figure is available in the online journal.)

images (cf. Wills-Davey & Thompson 1999; Dai et al. 2010). The instrument response functions (Howard et al. 2008) indicate that the maximum temperature response of the 195 Å passband is around $T_{195} = 10^{6.2}$ K. In the 171 Å passband, the peak response temperature is slightly lower, at $T_{171} = 10^{5.95}$ K, and the wave is still reasonably well defined. The 284 Å passband has several peaks in the temperature response, but most significantly at $T_{284} = 10^{6.3}$ K. Although observing a broad range of temperatures $T_{304} = 10^{4.9}$–$10^{6.3}$ K, the 304 Å passband is sensitive mostly to the lower transition region plasma at $T_{304} = 10^{4.9}$, and the EIT wave is mainly a coronal phenomenon (Wills-Davey & Thompson 1999; Zhukov & Auchère 2004; Long et al. 2008).

The large contrast of the wave to the background emission in the 195 Å passband observations, compared to that observed in the other passbands, suggests that the plasma compressed by the wave is emitting at around 1.5 MK. The wave is still visible in the 171 Å (≃1.0 MK) and 284 Å (≃2.0 MK) observations,

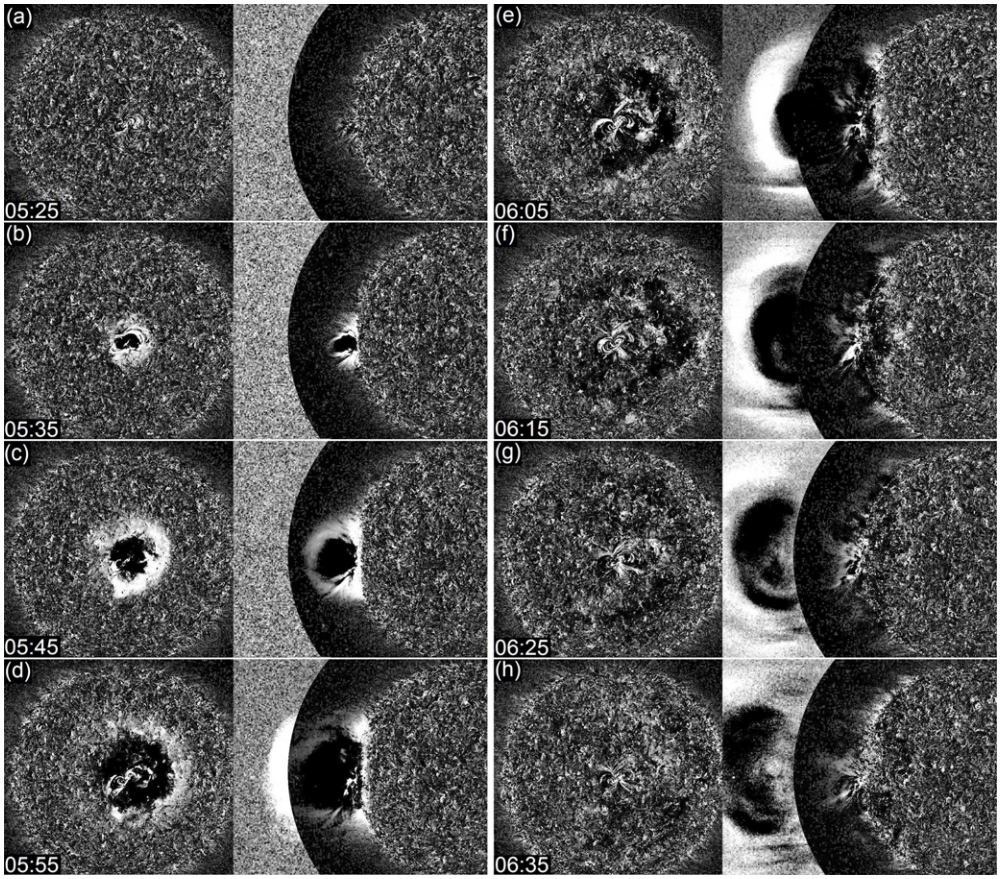

Figure 3. Running difference images of the EIT wave from the EUVI 195 Å *STEREO B* (on disk) and *STEREO A* (on-limb) telescopes. The *STEREO A* images are overlaid on COR1 coronagraph images. The running difference images were created by subtracting the previous image from the current image. White pixels indicate an increase in emission, black a decrease, and gray indicates no change. Images (a)–(h) are taken at increasing times, with a cadence of approximately 10 minutes.

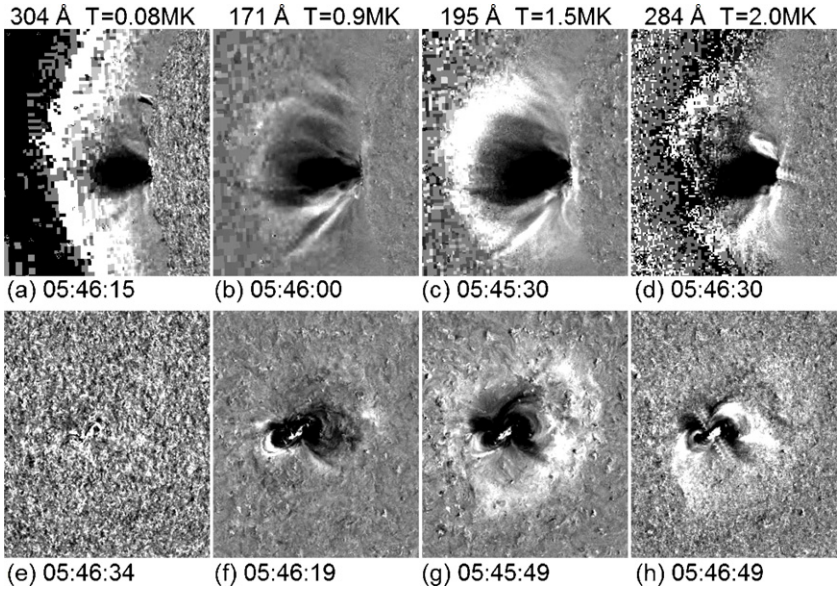

Figure 4. Images of the EIT wave in the four ST-A (top) and ST-B (bottom) EUVI passbands. The images were taken around 05:45 UT using a percentage difference method where the image of interest has a base image subtracted, and then divided through by the base image. The images are shown in ascending temperature order from left to right and have the same contrast scalings. The bright white pixelated regions above the limb are a compression artifact (especially visible in the 304 A ST-A image).

which may be due to the wave having a broad temperature range, or the response functions at these wavelengths are broad and cover the 1.5 MK temperature range, but with significantly lower count rates. The wave being visible in three coronal bandpasses is good evidence for the wave being a density perturbation. This interpretation is consistent with the compressive fast-magnetosonic wave model, whereby the wave travels though the corona, locally compressing the plasma and thus increasing

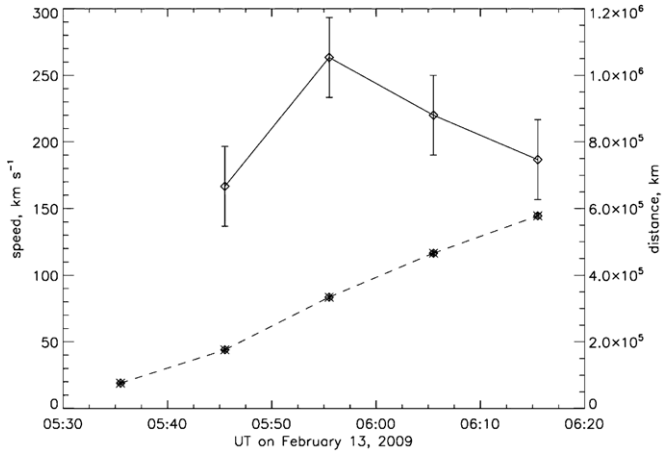

Figure 5. Change of distance (dashed line) and speed (solid) with time of the EIT wave traveling to the west of NOAA AR 1012.

the plasma emission. As a consequence the wave seems to be formed around 1.5 MK, and due to the weaker emission in the 171 Å and 284 Å passbands, we can apply a rather liberal error to this estimate of ±0.5 MK.

At this time the surrounding quiet corona exhibited little activity (e.g., ARs, coronal holes, etc.), and the wave was able to travel freely away from its source in all directions. ST-B 195 Å images were used to measure the wave speed. Each measurement of the wave was made at the front of the wave (furthest bright emission from the AR) as it propagated to the east (in the direction of the EIS slit position, see below). The wave could be followed in five successive images in the 195 Å bandpass before it was no longer distinguishable, and by measuring the change in distance over time between subsequent images, an average wave speed could be calculated. The position and speed profile can be seen in Figure 5, where the dashed line plot represents the change in distance between two recorded points with time, and the solid line represents the change in speed with time. Although the EUVI data in the 171 Å bandpass were taken at a higher cadence, the wave propagation is more difficult to measure in this bandpass due to the lower contrast of the wave with respect to the background. This is especially true for locations far from the erupting AR, where the EIS observations were taken (see below). The positional error is estimated to be ±2 pixels, due to the original images (2048 × 2048 pixels) being rebinned to 1024 × 1024 pixels. Rebinning the image helps when measuring the position of the wave front by reducing the noise (see Zhukov et al. 2009 for further discussion). In the following calculations, we use the measurement of the EIT wave speed around 06:05 UT, namely 220 ± 30 km s^{-1}. At this moment, the wave reached the region of interest in the quiet Sun observed by EIS.

3.2. Hinode/EIS Observations

At approximately 06:03 UT on 2009 February 13, EIS was performing a job composed of one 90 s exposure. The slit was centered on solar coordinates $X = 1''$ and $Y = 14''$, and observing a $1'' \times 256''$ field of view. *Hinode* is in a Sun-synchronous orbit around the Earth and as a consequence at this time was observing at an angle of 45° with respect to both ST-A and ST-B. The EIS slit position superimposed on a *Hinode* X-Ray Telescope (XRT; Golub et al. 2007) image can be seen in Figure 6 (bottom left). The top left and right images of Figure 6 show the EIS slit superimposed on the ST-B and ST-A EUVI 195 Å difference images, respectively, at similar times. The slit appears curved when superimposed on the EUVI images due to projection effects. A density diagnostic was done using the Si x λλ258/261 line ratio and the CHIANTI database (version 6.0.1; Dere et al. 1997a, 2009). It is useful to note that Si x lines have a similar formation temperature to the strongest line in the EUVI Fe xii 195 Å bandpass, providing a fairly accurate density measurement of the plasma detected in EUVI. Unfortunately, there was no temperature sensitive line ratio observed with EIS at this time.

The EIS pixels were binned into groups of five along the EIS slit (Y) direction and the spectra produced after binning were used to derive the electron density (Figure 7, see diamonds). We then summed the spectrum along the whole slit to increase the photon statistics and reduce the error bar. This new density can then be considered as an average over the slit. Its value is $3.4 \times 10^8 \mathrm{cm}^{-3}$, with an error bar ranging from $2.6 \times 10^8 \mathrm{cm}^{-3}$ to $4.2 \times 10^8 \mathrm{cm}^{-3}$, giving a relative error of ≈20%.

3.3. MDI Observations

The Michelson Doppler Imager (MDI) on *SOHO* (Scherrer et al. 1995) is capable of measuring line-of-sight magnetic field strengths in the photospheric regions. An MDI image from 04:51 UT, with the position of the EIS slit superimposed, is included in Figure 6(d) for comparison. By projecting the position of the EIS slit onto the MDI image, measurements of the field strength were recorded at similar latitudes and longitudes to the EIS slit. MDI recorded an average value of the photospheric magnetic field to be 7 ± 21 G. The bipolar field in the AR can be readily identified to the east of the superimposed EIS slit.

4. RESULTS

Using the observational results presented in the previous section ($T = (1.5 \pm 0.5) \times 10^6$ K, $n = (3.4 \pm 0.8) \times 10^8$ cm^{-3} and $v_f = 220 \pm 30$ km s^{-1}), the quiet-Sun sound speed is calculated to be $c_s = 200 \pm 30$ km s^{-1}. Because the observed EIT wave speed exceeds the local sound speed, Equation (3) can be used to calculate the quiet-Sun magnetic field strength. We calculate the field strength to be $B = 0.7 \pm 0.7$ G. The field strength can then be used with Equation (5) to calculate the plasma beta, which is found to be $\beta = 6.4 \pm 3.1$.

By taking a range in temperature and density, and assuming our recorded wave speed to be correct, a range in magnetic field values can be calculated as a function of temperature and density. The results are presented as a contour plot in Figure 8. It is noted that the sound speed is proportional to the square root of the temperature, and at ≃1.77 MK the sound speed equals the measured wave speed. Beyond this temperature the fast magnetosonic formalism is not valid, as the thermal speed exceeds the measured speed. The box overplotted in Figure 8 shows the range of density and temperature within our observational error bars.

Due to the large range of previously recorded EIT wave speeds, we considered it insightful to see how the calculated magnetic field varied with speed. Therefore, the range of speeds recorded in Thompson & Myers (2009) (15–654 km s^{-1}) were used with varying density and a constant temperature of 1.5×10^6 K to calculate a range of magnetic field strengths. Figure 9 shows how the magnetic field strength varies with wave speed and density. Similarly, Figure 10 shows how the calculated magnetic field varies with wave speed and temperature, with a constant density of $n = 3.4 \times 10^8$ cm^{-3}.

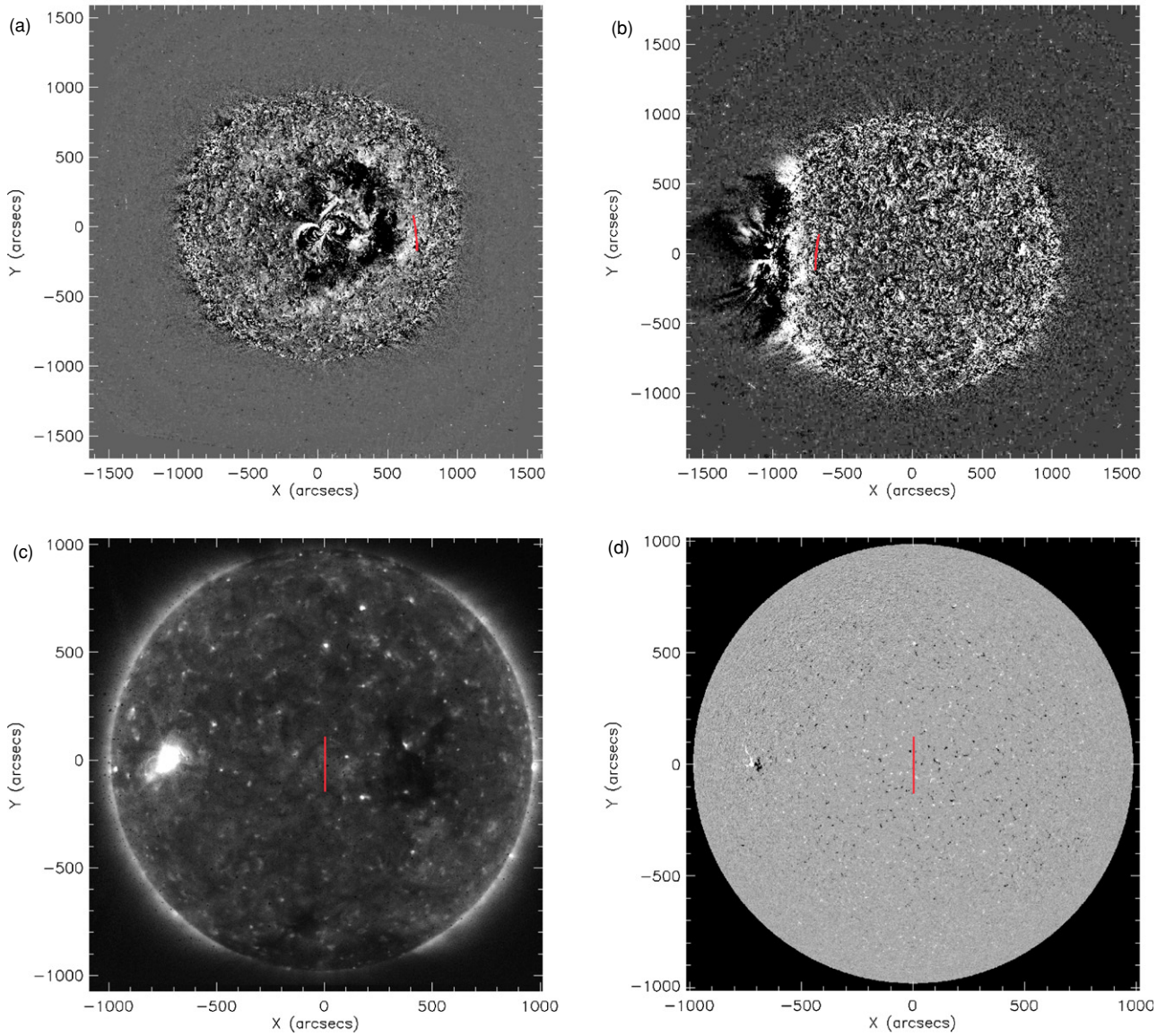

Figure 6. EIS slit superimposed on ST-B at 06:05 UT (a) and ST-A at 06:05 UT (b) EUVI 195 Å difference images. Panels (c) and (d) show the EIS slit superimposed on an XRT image at 06:03 UT and an MDI image at 04:51 UT, respectively.

5. DISCUSSION

We have used observations of an EIT waves speed, temperature, and density, and calculated the quiet-Sun magnetic field strength to be $B = 0.7 \pm 0.7$ G. It is difficult to compare our result with most other measurements of the coronal field strength, as most methods of deriving the field strength rely on the presence of strong magnetic fields, such as those found in ARs. Coronal seismology often relies on the identification and observation of individual oscillating loops/loop bundles. Such loops are mainly found in and around ARs, and have been observed to have field strengths between 10 and 40 G (see Verwichte et al. 2004, 2009; Van Doorsselaere et al. 2008). Also Ofman & Wang (2008) estimated the field in a multi-threaded loop structure following a filament eruption to be 20 ± 7 G. Dulk & McLean (1978) made estimates of the magnetic field above ARs, through a simple formalism describing the variation of magnetic field with height ($B = 0.5[(R/R_{\odot}) - 1]^{-1.5}$ for heights $1.02 \lesssim R/R_{\odot} \lesssim 10$). At 0.07 $R_{\odot}$, the field strength would be $\simeq$25 G. A value confirmed by Rabin et al. (1991), who calculated the magnetic field to be around 25 G. All these values exceed our estimate of our quiet-Sun magnetic field strength.

Vršnak et al. (2002) used the phenomenon of band splitting in type II bursts as a diagnostic for the magnetic field in the corona, and estimated the magnetic field strength to be $B \approx 5$ G at a height of 1.6 $R_{\odot}$, decreasing to $\approx$ 0.6 G at 2.5 $R_{\odot}$. Cho et al. (2007) used a similar technique and estimated the magnetic field strength to decrease from 1.3 to 0.6 G over the height range 1.6–2.1 $R_{\odot}$. However, it is noted that the EUVI 195 Å passband observes the corona up to 1.4 $R_{\odot}$, and consequently our estimated field strengths are likely to originate from observational heights lower in the solar atmosphere than those made with type II bursts.

We used MDI data to derive the average photospheric magnetic field strength to be $\sim$7 G, and our calculated coronal magnetic field value is $\sim$1 G. We now compare our results with the coronal magnetic field values predicted by simple models based on the measured photospheric field, e.g., the thin flux tube model (note though that it is usually applied to the magnetic field in the photosphere, see, e.g., Solanki et al. 1999), and a model

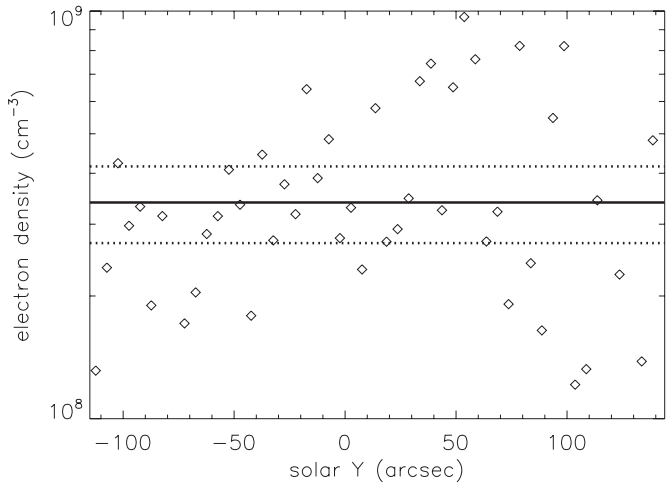

Figure 7. *Hinode*/EIS density diagnostic using the Si x λλ258/261 line ratio. Diamonds show the density along the EIS slit derived when summing over five spatial pixels. To improve the line statistics, we summed the profiles over all the pixels along the slit. The resulting density corresponds to the solid line, with dotted lines delimiting the error bar.

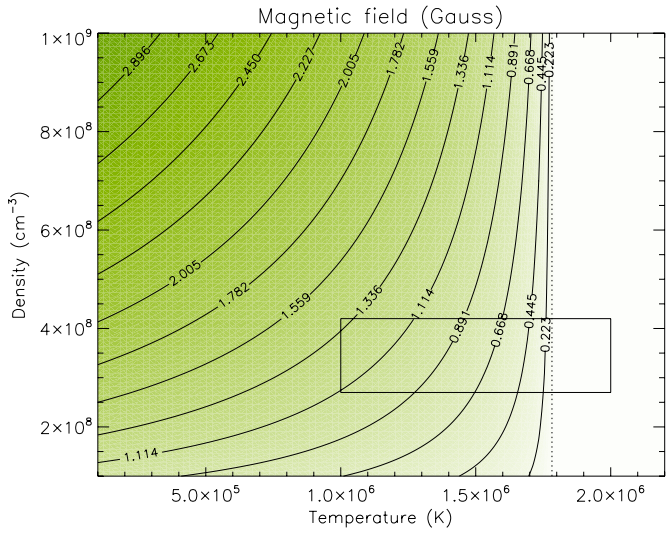

Figure 8. Magnetic field estimates for varying density and temperature. Each contour represents the magnetic field estimate for the given density and temperature calculated using the wave speed $v = 220\,\mathrm{km\,s^{-1}}$, the overplotted box highlights the region determined by the calculated errors in the density and the estimated temperature range. The dashed line indicates the temperature where the sound speed equals the recorded speed. Beyond this temperature the fast-mode approximation is invalid for the EIT wave considered in this study.

(A color version of this figure is available in the online journal.)

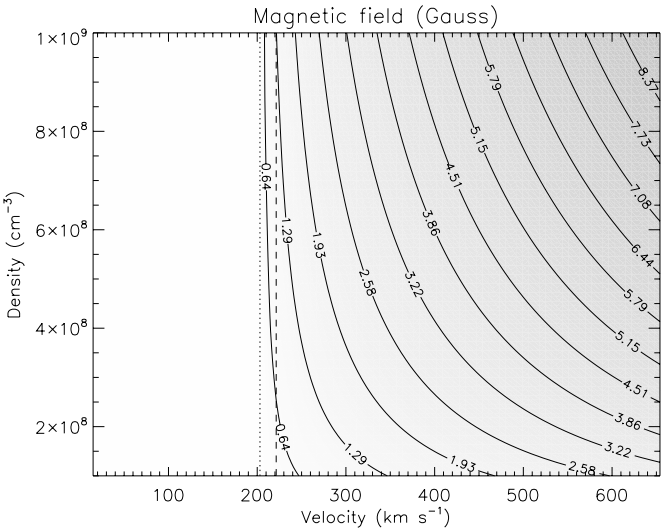

Figure 9. Magnetic field estimates for varying density and speed. Each contour represents the magnetic field estimate for the given density and speed calculated using a temperature, $T = 1.5 \times 10^6$ K. The dashed line represents our calculated speed ($v = 220\,\mathrm{km\,s^{-1}}$). The sound speed is represented by the dotted line, below this speed the fast-mode approximation is invalid.

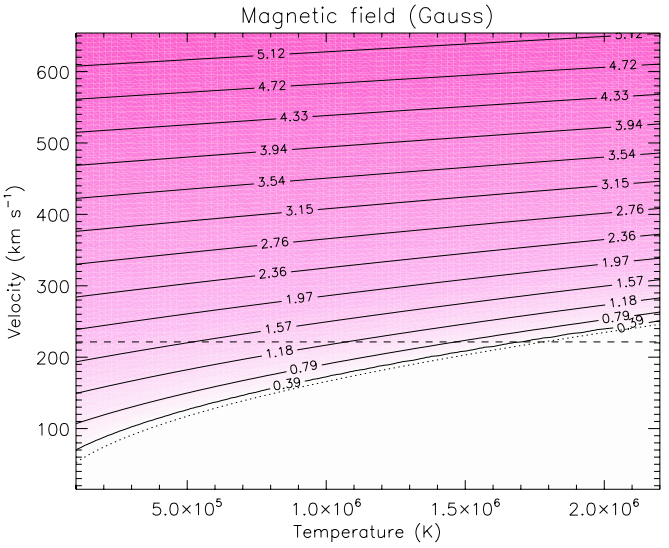

Figure 10. Magnetic field contours for varying values of speed and temperature, calculated using a fixed density of $n = 3.4 \times 10^8$ cm^{-3}. The dashed line represents our calculated speed ($v = 220\,\mathrm{km\,s^{-1}}$). The sound speed as a function of temperature is represented by the dotted line, below this line the fast-mode approximation is invalid.

(A color version of this figure is available in the online journal.)

of expanding magnetic field in plumes (Suess et al. 1998). In the thin flux tube approximation, the magnetic field drops exponentially with height, with a scale height double that of the pressure (Solanki et al. 1999). The wave traveling along the limb in ST-A image is visible in the height range between 0 and ∼0.2 $R_\odot$ (see Figure 6). Then, we can assume that the integration of the emission along the line of sight in the simultaneous ST-B image takes place along this height range. To get an order of magnitude estimate, we can assume that our calculated coronal magnetic field value refers to a height around half of the range, i.e., to 0.1 $R_\odot$.

Assuming a hydrostatic pressure scale height of 70 Mm (corresponding to the temperature of 1.5 MK), the photospheric field $B \sim 7$ G produces a coronal magnetic field strength of 4 G at a height of 0.1 $R_\odot$. For a purely radial decrease of the magnetic field, in a spherical geometry, the coronal field would be around 6 G. The Suess et al. (1998) model predicts an expansion factor of ∼13 at this height, resulting in a coronal field strength of 0.4 G, using the same parameters. This latter estimate is remarkably close to our calculated value of 0.7 G and may suggest that we are deriving the magnetic field in an expanding coronal flux tube. Assuming a photospheric field strength of ∼30 G (close to the upper value observed by MDI in our observations), the thin flux tube model predicts a coronal field strength of 18 G, and the Suess et al. (1998) model predicts a field strength of 2 G.

Our derivation of the field is based around the assumption that the EIT wave is in fact a linear fast magnetosonic wave. As discussed previously there is significant evidence for such

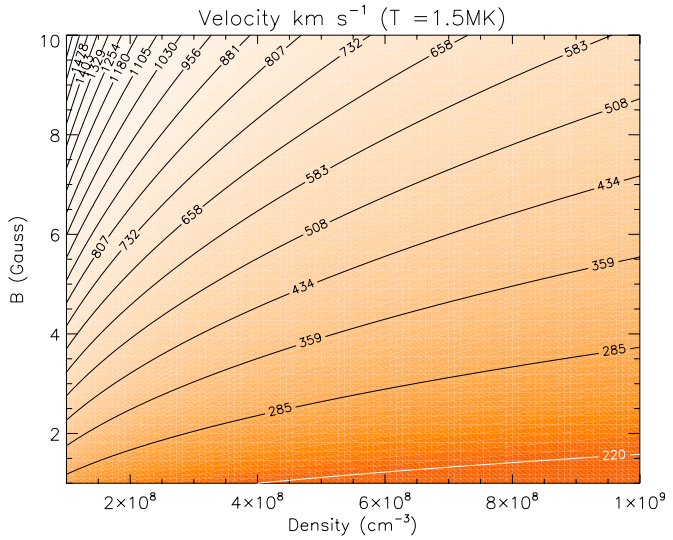

Figure 11. Contour plot showing calculated fast-mode wave speeds for varying density and magnetic field. Each speed is calculated using a temperature $T = 1.5 \times 10^6$ K. A contour corresponding to the observed speed of $v_f \approx 220\,\mathrm{km\,s^{-1}}$ is highlighted as a white line.

(A color version of this figure is available in the online journal.)

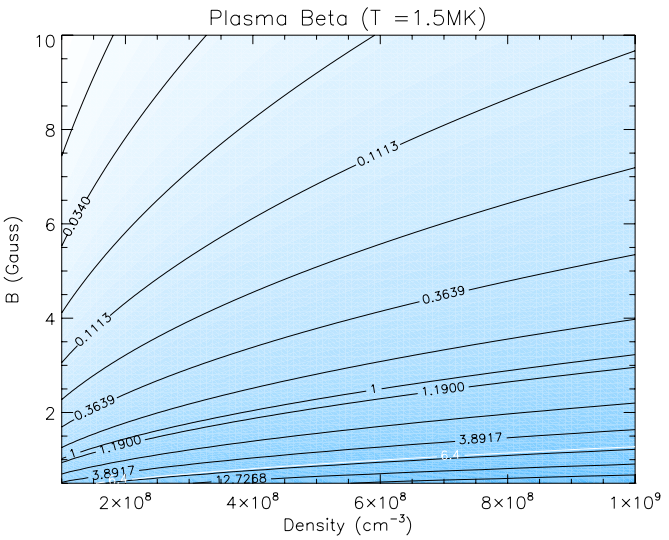

Figure 12. Contour plot of plasma beta values. Each value is calculated for a given density and magnetic field strength. The white contour represents a value of $\beta = 6.4$, which corresponds to our estimate of the plasma beta.

(A color version of this figure is available in the online journal.)

a hypothesis for this event, which has been corroborated with observations from several authors (e.g., Patsourakos & Vourlidas 2009; Kienreich et al. 2009). However, it was seen in Figure 8 that at $T \approx 1.7$ MK the sound speed equals the measured EIT wave speed ($\simeq$220 km s^{-1}) and as a consequence the magnetic field strength and Alfvén speed in Equation (2) tends to zero, and the wave becomes purely a sound wave. Therefore, if the temperature is increased beyond 1.7 MK, the linear fast magnetosonic formalism becomes invalid. For the fast-mode wave approximation to be valid, the observed wave speed should be greater than the local sound speed.

The linear fast magnetosonic approximation also relies upon small perturbations being introduced to the pressure, density, and magnetic field. These perturbations have to be finite but small so that only linear terms are retained in the resulting wave equations. Because the wave is visible in three coronal bandpasses, this is good evidence for the wave being a density perturbation.

In this study, the magnetic field is assumed to be largely perpendicular to the solar surface, and such a scenario might be encountered lower down in the solar atmosphere. In reality, the wave is not restricted to a two-dimensional plane and will propagate in various directions and encounter the surrounding field at various angles (Veronig et al. 2010). However, we are justified in using this assumption in an optically thin medium, as the greatest emission will come from the greatest amount of emitting material. *STEREO* observes the EIT wave at heights between 0 and 0.2 $R_\odot$ above the solar surface; this will be toward the base of the expanding bubble (Ma et al. 2009), at a height where a large proportion of the field is assumed to be perpendicular. A percentage of non-radial field will lower the speed of the wave, and as a consequence lower our estimation of the magnetic field. Therefore, our quoted values should be seen as an upper limit. It is also noted that a percentage of non-radial field and regions of varying magnetic field strength will also act to broaden the wave front, which may go some way to explaining the broad bright fronts observed.

The magnetic field calculation also relied on several calculated coronal parameters, the EIT wave speed ($v_f \approx$ 220 km s^{-1}) recorded in the *STEREO* EUVI Fe XII 195 Å passband ($T \approx 1.5 \times 10^6$ K) and the coronal density ($n \approx 3.4 \times 10^8$ cm^{-3}) measured with EIS in the same temperature regime.

The fast-mode wave theory can be used to estimate wave speeds for varying values of density and magnetic field strength, this is shown in Figure 11. The corresponding plot for the plasma beta is shown in Figure 12. A white contour line corresponding to the speed $v_f \approx 220\,\mathrm{km\,s^{-1}}$ is included to highlight where our recorded speed fits in. It is clearly seen that for a reasonable range of density and magnetic field strength values, a large range of wave speeds are produced. This range in wave speeds may help explain the large variation of observed EIT and Moreton wave speeds.

Figures 9 and 10 compare the range of speeds (15–654 km s^{-1}) presented in Thompson & Myers (2009) with density and temperature, respectively. Estimates of the magnetic field strength could only be calculated for EIT wave speeds above the local sound speed, which was approximately 200 km s^{-1} in our case. One hundred seven of the 158 plane-of-sky speeds recorded by Thompson & Myers (2009) were below this value suggesting that less than half can be treated as fast-mode MHD waves. However, if we assume that not all waves are going to be observed at the same temperature, and use our lower estimate for the wave temperature, 1×10^6 K ($c_s = 166\,\mathrm{km\,s^{-1}}$), we find only 82 of the 158 plane-of-sky speeds fall below the sound speed threshold, of which 69 are classed as "low reliability" or "very low reliability."

The density measurements used in our work were taken close to the center of the solar disk and were averaged to reduce any error recorded from a single position. This value corresponds well with previous measurements, for example, Young (2005) estimates the density in the lower corona quiet Sun to be $\approx 10^{8.6}$ cm^{-3}, which is slightly larger than our density estimates, but of a similar order of magnitude.

The temperature estimates are based around the argument that the wave is predominantly observed in quiet-Sun regions, where plasma lies in the 1–2 MK temperature range and where the peak of the 195 Å passband lies Howard et al. (2008). The wave is also observed reasonably well in 171 Å observations,

which have a peak temperature around 1 MK, but with a large, but not dominant, contribution to the emission made by the 1.5 MK plasma. The wave is also observed in the 284 Å passband, the temperature of which is composed of several peaks between 0.5 MK and a dominant peak at 2.5 MK. Therefore, it is expected that if the wave is mainly formed around 1.5 MK, that it will also be seen in the 284 Å passband. However, it should be noted that the instrument sensitivity is lower at this temperature, and records an order of magnitude less photons per second than the 195 Å passband (Howard et al. 2008).

One surprising aspect of our results is the calculated plasma beta. Figure 12 shows the variation of plasma beta for a range of density and magnetic field values. This value is often assumed to be less than unity allowing the magnetic field to dictate the state of the corona (Gary 2001). Our results indicate a larger value of $\beta = 6 \pm 3$. This means that the magnetic field cannot constrain the plasma in the low corona. Due to the outward-directed plasma pressure gradient force, the quiet-Sun corona should then expand in the interplanetary space as the solar wind. This intriguing possibility needs future investigations, both through observations and modeling.

These results show that multi-instrument observations of EIT waves provide an effective method for estimating coronal properties through coronal seismology. If it was not for the unique position of the *STEREO* satellites at this time, and the fortuitous measurement of the coronal plasma density with quasi-simultaneous EIS observations, the estimates of the magnetic field strength presented here would be unattainable.

6. CONCLUSIONS

We used *STEREO* EUVI observations of 2009 February 13 EIT wave event, in conjunction with EIS density measurements, to estimate the quiet-Sun coronal magnetic field strength. We measured the EIT wave speed to be $\simeq 220 \pm 30\,\mathrm{km\,s^{-1}}$, which was mainly observed at temperatures around 1.5 MK. At a similar time EIS made measurements of the spectra which allowed us to calculate the quiet-Sun density in a region into which the wave subsequently traveled. The EIS measurements were made for a plasma at a similar temperature to the peak response temperature of the 195 Å passband of the EUVI observations ($\simeq$1.5 MK) and the estimated density was $n \approx (3.4 \pm 0.8) \times 10^8\ \mathrm{cm^{-3}}$. By assuming the wave was a fast magnetosonic wave in nature, we were able to use our measurements to estimate the coronal magnetic field to be $B \simeq 0.7 \pm 0.7$ G. The corresponding value of the plasma beta (6 ± 3) is too high for plasma to be constrained by the quiet-Sun magnetic field.

We acknowledge support from the Belgian Federal Science Policy Office through the ESA-PRODEX program. The *STEREO*/SECCHI data used here were produced by an international consortium of the Naval Research Laboratory (USA), Lockheed Martin Solar and Astrophysics Lab (USA), NASA Goddard Space Flight Center (USA), Rutherford Appleton Laboratory (UK), University of Birmingham (UK), Max-Planck-Institut for Solar System Research (Germany), Centre Spatiale de Liège (Belgium), Institut dOptique Théorique et Appliquée (France), and Institut dAstrophysique Spatiale (France). MDI data have been used courtesy of the *SOHO*/MDI consortium. *SOHO* is a project of international cooperation between ESA and NASA. *Hinode* is a Japanese mission developed and launched by ISAS/JAXA, with NAOJ as a domestic partner and NASA and STFC (UK) as international partners. It is operated by these agencies in cooperation with ESA and NSC (Norway). CHIANTI is a collaborative project involving researchers at NRL (USA), RAL (UK), and the universities of Cambridge (UK), George Mason (USA), and Florence (Italy).

Facilities: STEREO, *SOHO*, *Hinode*

REFERENCES

Banerjee, D., Erdélyi, R., Oliver, R., & O'Shea, E. 2007, Sol. Phys., 246, 3
Biesecker, D. A., Myers, D. C., Thompson, B. J., Hammer, D. M., & Vourlidas, A. 2002, ApJ, 569, 1009
Cargill, P. J. 2009, Space Sci. Rev., 144, 413
Chen, P. F., Wu, S. T., Shibata, K., & Fang, C. 2002, ApJ, 572, L99
Cho, K., Lee, J., Gary, D. E., Moon, Y., & Park, Y. D. 2007, ApJ, 665, 799
Cohen, O., Attrill, G. D. R., Manchester, W. B., & Wills-Davey, M. J. 2009, ApJ, 705, 587
Culhane, J. L., et al. 2007, Sol. Phys., 243, 19
Dai, Y., Auchère, F., Vial, J., Tang, Y. H., & Zong, W. G. 2010, ApJ, 708, 913
Delaboudinière, J., et al. 1995, Sol. Phys., 162, 291
Delannée, C., Török, T., Aulanier, G., & Hochedez, J. 2008, Sol. Phys., 247, 123
De Moortel, I., & Pascoe, D. J. 2009, ApJ, 699, L72
Dere, K. P., Landi, E., Mason, H. E., Monsignori Fossi, B. C., & Young, P. R. 1997a, A&AS, 125, 149
Dere, K. P., Landi, E., Young, P. R., Del Zanna, G., Landini, M., & Mason, H. E. 2009, A&A, 498, 915
Dere, K. P., et al. 1997b, Sol. Phys., 175, 601
Dulk, G. A., & McLean, D. J. 1978, Sol. Phys., 57, 279
Gallagher, P. T., & Long, D. M. 2010, Space Sci. Rev., 135
Gary, G. A. 2001, Sol. Phys., 203, 71
Golub, L., et al. 2007, Sol. Phys., 243, 63
Gopalswamy, N., et al. 2009, ApJ, 691, L123
Handy, B. N., et al. 1999, Sol. Phys., 187, 229
Howard, R. A., et al. 2008, Space Sci. Rev., 136, 67
Kaiser, M. L., Kucera, T. A., Davila, J. M., St. Cyr, O. C., Guhathakurta, M., & Christian, E. 2008, Space Sci. Rev., 136, 5
Kienreich, I. W., Temmer, M., & Veronig, A. M. 2009, ApJ, 703, L118
Lin, H., Kuhn, J. R., & Coulter, R. 2004, ApJ, 613, L177
Lin, H., Penn, M. J., & Tomczyk, S. 2000, ApJ, 541, L83
Liu, Y., & Lin, H. 2008, ApJ, 680, 1496
Long, D. M., Gallagher, P. T., McAteer, R. T. J., & Bloomfield, D. S. 2008, ApJ, 680, L81
Ma, S., et al. 2009, ApJ, 707, 503
Metcalf, T. R., et al. 2008, Sol. Phys., 247, 269
Moreton, G. E. 1960, AJ, 65, 494
Moses, D., et al. 1997, Sol. Phys., 175, 571
Nakariakov, V. M., Ofman, L., Deluca, E. E., Roberts, B., & Davila, J. M. 1999, Science, 285, 862
Ofman, L., & Wang, T. J. 2008, A&A, 482, L9
Patsourakos, S., & Vourlidas, A. 2009, ApJ, 700, L182
Rabin, D. M., Devore, C. R., Sheeley, N. R., Jr., Harvey, K. L., & Hoeksema, J. T. 1991, in The Solar Activity Cycle, ed. A. N. Cox, W. C. Livingston, & M. S. Matthews (Tucson, AZ: Univ. Arizona Press), 781
Ramesh, R., Kathiravan, C., & Sastry, C. V. 2010, ApJ, 711, 1029
Roberts, B., Edwin, P. M., & Benz, A. O. 1984, ApJ, 279, 857
Scherrer, P. H., et al. 1995, Sol. Phys., 162, 129
Schmidt, J. M., & Ofman, L. 2010, ApJ, 713, 1008
Schrijver, C. J., & De Rosa, M. L. 2003, Sol. Phys., 212, 165
Solanki, S. K., Finsterle, W., Rüedi, I., & Livingston, W. 1999, A&A, 347, L27
Subramanian, K. R., Ebenezer, E., & Raveesha, K. H. 2010, in Magnetic Coupling Between the Interior and Atmosphere of the Sun, ed. S. S. Hasan & R. J. Rutten (Berlin: Springer), 482
Suess, S. T., Poletto, G., Wang, A.-H., Wu, S. T., & Cuseri, I. 1998, Sol. Phys., 180, 231
Thompson, B. J., & Myers, D. C. 2009, ApJS, 183, 225
Thompson, B. J., Plunkett, S. P., Gurman, J. B., Newmark, J. S., St. Cyr, O. C., & Michels, D. J. 1998, Geophys. Res. Lett., 25, 2465
Thompson, B. J., et al. 1999, ApJ, 517, L151
Thompson, W. T., et al. 2003, Proc. SPIE, 4853, 1
Uchida, Y. 1968, Sol. Phys., 4, 30
Uchida, Y. 1970, PASJ, 22, 341
Uchida, Y., Altschuler, M. D., & Newkirk, G., Jr. 1973, Sol. Phys., 28, 495
Van Doorsselaere, T., Nakariakov, V. M., Young, P. R., & Verwichte, E. 2008, A&A, 487, L17
Veronig, A. M., Muhr, N., Kienreich, I. W., Temmer, M., & Vršnak, B. 2010, ApJ, 716, L57

Verwichte, E., Aschwanden, M. J., Van Doorsselaere, T., Foullon, C., & Nakariakov, V. M. 2009, ApJ, 698, 397
Verwichte, E., Nakariakov, V. M., Ofman, L., & Deluca, E. E. 2004, Sol. Phys., 223, 77
Vršnak, B., Magdalenić, J., Aurass, H., & Mann, G. 2002, A&A, 396, 673
Wang, Y. 2000, ApJ, 543, L89
Wang, Y., & Sheeley, N. R., Jr. 1992, ApJ, 392, 310
Warmuth, A., Vršnak, B., Aurass, H., & Hanslmeier, A. 2001, ApJ, 560, L105
Wills-Davey, M. J., & Attrill, G. D. R. 2009, Space Sci. Rev., 149, 325
Wills-Davey, M. J., & Thompson, B. J. 1999, Sol. Phys., 190, 467
Wuelser, J., et al. 2004, Proc. SPIE, 5171, 111
Wu, S. T., Zheng, H., Wang, S., Thompson, B. J., Plunkett, S. P., Zhao, X. P., & Dryer, M. 2001, J. Geophys. Res., 106, 25089
Young, P. R. 2005, A&A, 439, 361
Zhukov, A. N., & Auchère, F. 2004, A&A, 427, 705
Zhukov, A. N., Rodriguez, L., & de Patoul, J. 2009, Sol. Phys., 259, 73